



# **Influence of station density and multi-constellation GNSS observations on troposphere tomography**

Qingzhi Zhao<sup>1</sup>, Kefei Zhang<sup>2,3</sup> and Wanqiang Yao<sup>1</sup>

<sup>1</sup>College of Geomatics, Xi'an University of Science and Technology, Xi'an, China.

<sup>2</sup>School of Environment Science and Spatial Informatics, China University of Mining and  
Technology, Xuzhou, China

<sup>3</sup>Satellite Positioning for Atmosphere, Climate and Environment (SPACE) Research Centre, RMIT  
University, Melbourne, Australia

**Abstract:** Troposphere tomography, using multi-constellation GNSS observations, has become a novel approach for the three-dimensional (3-d) reconstruction of water vapour fields. An analysis of the integration of four Global Navigation Satellite Systems (BeiDou, GPS, GLONASS and Galileo) observations is presented to investigate the impact of station density and single/multi-constellation GNSS observations on troposphere tomography. Additionally, the optimal horizontal resolution of research area is determined in Hong Kong, which considers both the number of voxels divided, and the coverage rate of discretized voxels penetrated by satellite signals. Tomography experiment reveals that the influence of station density in a GNSS network is more significant than the multi-constellation GNSS observations on the reconstruction of 3-d atmospheric water vapour profiles. Compared to the tomographic result from the multi-constellation GNSS (BeiDou, GPS, GLONASS and Galileo) observations, the RMS of SWD residuals derived from the single-GNSS observations has been decreased by 16% when the data from the other four stations are added. Furthermore, more experiments have been carried out to analyse the contributions of different combined GNSS data to the reconstructed results, and the comparisons show some interesting results: (1) the number of iterations used in determining the weighting matrices of different equations in tomography modelling can be decreased when considering multi-constellation GNSS observations; (2) the tomographic result with multi-constellation GNSS data can improve the reconstructed quality of 3-d atmospheric water vapour by the largest RMS value of about 11% when compared to the PPP-estimated SWD, but this was not as high as was expected.

**Keywords:** Tropospheric tomography; Multi-constellation GNSS; Station density; Atmospheric water vapour.

## **1. Introduction**

For some years, GNSS-based tropospheric tomography has been regarded as one of the most promising techniques with which to reconstruct the temporal-spatial variation of atmospheric water vapour (Flores et al., 2000; Grespi et al., 2008). By discretising the area of interest into some voxels in different directions, the water vapour information in divided voxels can be



38 reconstructed with assumption that the unknown estimated parameters are constant during a given  
39 period (Radon, 1917; Flores et al., 2000). So far, this technique has been proved by some  
40 feasibility studies with GPS-only observations (Troller, 2002; Bender and Raabe, 2007; Chen and  
41 Liu, 2014) as well as the simulated multi-constellation GNSS observation (Grespi et al., 2008;  
42 Bender et al., 2011; Wang et al., 2014; Benevides et al., 2015c; Benevides et al., 2017). In addition,  
43 the experimental result reveals that, compared to GPS-only observations, a greater improvement in  
44 the accuracy of tomographic water vapour information using the multi-constellation GNSS  
45 observation has been obtained (Bender et al., 2011; Benevides et al., 2015c; Benevides et al.,  
46 2017).

47 Due to the specific distribution of satellite signals, and the immovability of ground-based stations  
48 in regional network, the geometry of the observed-signal distribution is similar to an inverted cone,  
49 which has a negative effect on tropospheric tomography (Benevides et al., 2015a, 2015b). The  
50 main disadvantage caused by such phenomenon is the sparse filling of the discretised voxels at the  
51 edge and lower sections of the area of interest (Bender and Raabe, 2007). Optimising the design  
52 matrix of observation equation is a way to overcome such bad condition by selecting a  
53 non-uniform symmetrical division of horizontal voxels and a non-uniform thicknesses of the  
54 vertical voxel layers (Nilsson and Gradinarsky, 2006; Yao and Zhao, 2016a, 2016b). Imposing the  
55 satellite rays which come out from the side of the research area onto the reconstructed modelling  
56 is another effective way in which to optimise the structure of the design matrix (Yao and Zhao,  
57 2016b; Yao et al., 2016; Zhao and Yao, 2017). In addition, using more slant-path observations  
58 derived from the upcoming fully-operational GNSS constellations (BeiDou, GLONASS, and  
59 Galileo) is a possible way of solving such issue (Grespi et al., 2008; Bender et al., 2011;  
60 Benevides et al., 2017). Finally, increasing the density of the GNSS network also is a feasible way  
61 to improve the stability and structure of the design matrix (Nilsson and Gradinarsky, 2006).

62 In most past studies, multi-constellation GNSS observations are simulated with ideal data which  
63 cannot reflect the real conditions of multi-constellation GNSS observations, including the  
64 variations in latitudes, areas, topography, and the surroundings of GNSS stations (Nilsson and  
65 Gradinarsky, 2006; Grespi et al., 2008; Wang et al., 2014). Therefore, the preliminary result  
66 concluded from those studies needs further verification based on the observed multi-constellation  
67 GNSS data, which becomes the focus of this study. In this paper, a method is proposed to  
68 determine the optimal division of voxels in horizontal direction automatically according to the  
69 range of the tomography area as well as the number and distribution of GNSS stations. The  
70 influence of number of stations in a network on the tomographic result is then compared with the  
71 reconstructed wet refractivity field derived from multi-constellation GNSS observations. Finally,  
72 the quality and reliability of tomographic atmospheric water vapour obtained from the different  
73 combined multi-constellation GNSS observations is analysed.

74 The aim of this research is to analyse the importance and influence of station density and  
75 single/multi-constellation GNSS observations on tropospheric tomography in an upcoming future  
76 scenario of having the multi-constellation GNSS (GPS, BeiDou, GLONASS, and Galileo)  
77 constellations fully operational. The structure of this paper is organised as follows: Sect. II  
78 presents the theory of tropospheric tomography, Sect. III describes the experimental data and the  
79 determination of horizontal resolution. The importance and influence of station density and  
80 single/multi-constellation GNSS observations on troposphere tomography are detailed analysed  
81 and compared in Sects IV and V, respectively, and key conclusions are presented in Sect. VI.



82

## 83 2. GNSS tropospheric tomography

84 Generally, slant wet delay (SWD) and slant water vapour (SWV) are two types of input  
 85 observations used in building the observation equations, and the corresponding output results are  
 86 wet refractivity and water vapour density, respectively (Flores et al., 2000; Skone and Hoyle, 2005;  
 87 Notarpietro et al., 2011; Champollion et al., 2005). Two kinds of reconstructed output information  
 88 can be inter-converted with atmospheric temperature field information (Bender et al., 2011). In  
 89 this paper, the SWD is selected to reconstruct the atmospheric wet refractivity field.  
 90 The zenith tropospheric delay (ZTD) is estimated with high precision using the GNSS observation,  
 91 consists of two parts, which includes zenith wet delay (ZWD) and zenith hydrostatic delay (ZHD).  
 92 The former can be accurately estimated based on the empirical model, *e.g.*, Saastamoinen (1973),  
 93 with the observed surface pressure information. Therefore, the latter is obtained by subtracting the  
 94 ZHD from ZTD. In our study, the observed multi-constellation GNSS data are processed using the  
 95 multi-constellation GNSS Precise Point Positioning (PPP) software with precise orbit and clock  
 96 error products (Zhao et al., 2018). Consequently, the SWD can be expressed as:

$$97 \quad \text{SWD}_{azi,ele} = m_w(ele) \cdot \text{ZWD} + m_w(ele) \cdot \cot(ele) \cdot (G_{NS}^w \cdot \cos(azi) + G_{WE}^w \cdot \sin(azi)) \quad (1)$$

98 Where  $m_w$  is the wet mapping function. In our processing, the wet Vienna Mapping Function  
 99 (VMF) is adopted; *ele* refers to the satellite elevation angle while *azi* represents the azimuth  
 100 angle.  $G_{NS}^w$  and  $G_{WE}^w$  are the north-south and west-east gradients of wet delay, respectively,  
 101 which are caused by the non-isotropic nature of atmospheric water vapour distributions (Bi et al.,  
 102 2006).  
 103 The SWD value from the satellite to GNSS station antenna is an integral expression, given by:

$$104 \quad \text{SWD} = 10^{-6} \cdot \int N_w(s) ds \quad (2)$$

105 Where  $N_w$  represents the wet refractivity (mm/km) and *s* is the distance over which the  
 106 satellite signal penetrates the troposphere (km). According to this tomographic technique, the area  
 107 of interest is divided into a number of voxels and the wet refractivity parameters are considered  
 108 unchanged during the selected period. Consequently, the total SWD value can be expressed as the  
 109 sum of discretised delay parts in each voxel along the satellite ray path, and a linear expression  
 110 can be listed as:

$$111 \quad \text{SWD} = \sum_{i=1}^m \sum_{j=1}^n \sum_{k=1}^p (a_{ijk} \cdot x_{ijk}) \quad (3)$$

112 Where *m* and *n* are the total number of voxels divided in longitudinal and latitudinal  
 113 directions while *p* is the total number in vertical direction, respectively;  $a_{ijk}$  is the distance of  
 114 satellite rays, and  $x_{ijk}$  is the unknown wet refractivity parameters in voxel  $(i, j, k)$ , respectively.  
 115 Therefore, the observation equation of tomography modelling can be established for all GNSS  
 116 stations in a network of interesting area.



As mentioned above, the geometric distribution of satellite rays in the tomographic area is an inverted cone, thus the design matrix of observation equations is a sparse matrix and not all of the unknown wet refractivity values are estimated. To solve the problem of rank deficiency, some external constraints are required (Flores et al., 2000; Troller et al., 2006; Rohm and Bosy., 2011). Two constraints are imposed in this paper, the one is horizontal weighted constraint, and the other is the vertical constraint based on the observed radiosonde data in the first three days of the reconstructed epoch. Consequently, the tomographic modelling imposed the following constraint equations:

$$\begin{pmatrix} \mathbf{A} \\ \mathbf{H} \\ \mathbf{V} \end{pmatrix} \cdot \mathbf{x} = \begin{pmatrix} \mathbf{y}_{swd} \\ \mathbf{0} \\ \mathbf{y}_{rs} \end{pmatrix} \quad (4)$$

Where  $\mathbf{H}$  represents to the horizontal coefficient matrices while  $\mathbf{V}$  refers to the vertical coefficient matrices, respectively.  $\mathbf{y}_{swd}$  is a vector with SWD values while  $\mathbf{y}_{rs}$  is the *a priori* information obtained from the radiosonde information. The form of solution of the unknown wet refractivity vector can be written as:

$$\hat{\mathbf{x}} = (\mathbf{A}^T \cdot \mathbf{P}_A \cdot \mathbf{A} + \mathbf{H}^T \cdot \mathbf{P}_H \cdot \mathbf{H} + \mathbf{V}^T \cdot \mathbf{P}_V \cdot \mathbf{V})^{-1} \cdot (\mathbf{A}^T \cdot \mathbf{P}_A \cdot \mathbf{y}_{swd} + \mathbf{V}^T \cdot \mathbf{P}_V \cdot \mathbf{y}_{rs}) \quad (5)$$

Where  $\mathbf{P}_A$ ,  $\mathbf{P}_H$ , and  $\mathbf{P}_V$  are the weighting matrices of observation, horizontal and vertical equation, respectively. The weighting matrices for different equations are determined by an optimal weighting method and the homogeneity test was adopted to verify the statistically equality of three kinds of *a posteriori* unit weight variances (Bartlett, 1937; Guo et al., 2016).

### 3. Tomography experiment and description

#### 3.1 Experimental data

A network consisting of fourteen GNSS Satellite Reference Stations (SatRef) in Hong Kong was selected to perform the tomography experiment during the period of Doy 4 to 26, 2017. The geographic locations of GNSS and radiosonde stations are presented in Fig. 1. The sampling interval of the GNSS observations used here was 30 s. The radiosonde station in the experimental area is used to test the reconstructed result of GNSS troposphere tomography. The range of tomographic region is from 113.87 °E to 114.35 °E and 22.18 °N to 22.54 °N while the vertical height is from 0 to 9 km. The horizontal resolution, in voxel terms, is  $4 \times 12$  in latitudinal and longitudinal directions as determined by an optimal voxel division method, which will be described below. The vertical resolution adopts a non-uniform vertical layer strategy (Yao and Zhao, 2016b) with two layers of a thickness of 500 m, three layers of 600 m, four layers of 800 m, and three layers of 1000 m from the ground to the top of tomography region.

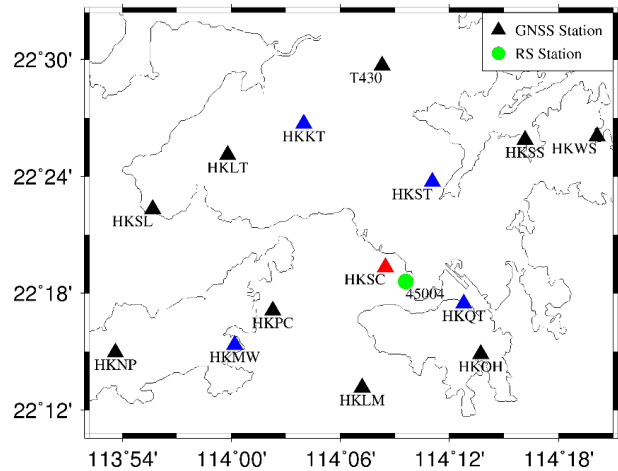


Fig. 1. Geographic location of GNSS and radiosonde stations in SatRef of Hong Kong. The blue triangles are used to increase the station density, while the station HKSC marked in red and radiosonde station 45004 marked in green are used to evaluate the performance of tomographic result

### 3.2 Determination of horizontal resolution

In the procedure of horizontal voxel division, an approach is developed which able to determine adaptively the optimal horizontal resolution according to the scope of tomography region as well as the number and distribution of GNSS stations. The specific principle is such that: increasing the coverage rate of voxels penetrated by satellite signals and optimising the design matrix of the observation equation, while considering a higher horizontal resolution to reflect the atmospheric water vapour distribution in as much detail as possible, therefore, a comparative experiment is performed to validate the developed approach of determining horizontal resolution. Nine schemes are designed (Table 1): the number of voxels for the bottom layers and the coverage rate of distributed stations located at the bottom layer are calculated. It can be concluded that Scheme 3 was optimal while considering both the number of voxels divided and the coverage rate of GNSS stations located in the bottom layers.

Table 1. Statistical result of determining horizontal resolution for nine schemes

Scheme	Longitude ×Latitude	Total voxels	Step of longitude	Step of latitude	Coverage rate of stations (%)
1	12×9	108	0.04	0.04	13.0
2	12×6	72	0.04	0.06	18.1
3	12×4	48	0.04	0.09	29.2
4	8×9	72	0.06	0.04	19.4
5	8×6	48	0.06	0.06	25.0
6	8×4	32	0.06	0.09	43.8
7	6×9	54	0.08	0.04	25.9
8	6×6	36	0.08	0.06	36.1
9	6×4	24	0.08	0.09	58.3



In addition, the coverage rate of the satellite rays for the entire research region is analysed for the date of day 4, 2017 under nine combined multi-constellation GNSS observations. In this study, the time period for each tomography is selected as five minutes. The specific statistical result is presented in Table 2, where G/C/R/E refer to GPS, BeiDou, GLONASS, and Galileo, respectively. The conclusion can be drawn that the coverage rate of satellite rays in Schemes 3, 6, 8, and 9 are relatively large. Considering the number of voxels and coverage rate of stations located in the bottom layers, Scheme 3 is also considered as the optimal choice. Apart from the above conclusion, it also can be concluded that the coverage rate of voxels penetrated by satellite signals for the entire region using two/three/four-GNSS observations are both increased with the minimum coverage rate by about 5%, when compared to the single-GNSS conditions.

Table 2. Coverage rate of satellite rays for nine combined multi-constellation GNSS observations  
 (Unit: %)

Scheme	1	2	3	4	5	6	7	8	9
G	51.3	60.8	72.7	61.0	69.8	81.4	67.2	76.0	85.8
C	50.0	61.2	73.9	57.4	68.5	80.6	62.2	72.6	82.5
R	44.0	54.4	67.7	53.5	62.9	78.0	61.5	71.5	84.1
E	30.9	40.3	53.1	40.0	50.6	64.9	47.0	57.7	72.1
GC	62.1	71.2	79.3	69.0	77.6	85.0	72.8	81.2	87.8
GR	60.4	68.8	79.5	68.0	75.8	85.2	73.1	80.9	88.5
CR	59.2	69.5	79.1	65.9	75.9	84.4	70.9	80.3	86.9
GCR	65.6	74.1	81.7	71.6	80.0	86.5	75.5	83.3	89.2
GCRE	66.9	75.3	82.3	72.5	80.5	86.8	76.1	83.6	89.5

182

#### 183 4. Importance and influence of station density and 184 multi-constellation GNSS observations on tropospheric 185 tomography

In this section, two schemes are designed to analyse the importance and influence of station density and multi-constellation GNSS data on the reconstructed atmospheric wet refractivity. For Scheme 1, all fourteen GNSS stations, as presented by triangles of different colour in Figure 1, are selected for this tomographic experiment but only considering single-GNSS observations (GPS, BeiDou, GLONASS, and Galileo, respectively), which are abbreviated to G-14, C-14, R-14, and E-14, respectively, and the 14 refers to the number of stations used for tomography. For Scheme 2, only ten GNSS stations are used, as shown by the nine black triangles and one red triangle in Figure 1, but considering the different multi-constellation GNSS combinations, those combinations are abbreviated to GC-10, GR-10, CR-10, GCR-10, and GCRE-10, respectively. The following analysis is focussed on: (1) the investigating of two schemes in the number of GNSS rays used and coverage rate of the voxels penetrated by GNSS rays, respectively; (2) the comparison of reconstructed result with radiosonde data as well as the PPP-estimated SWD values of stations HKSC, respectively.

##### 199 4.1 Comparison of GNSS rays used and the coverage rate of voxels penetrated

200 23 days of data during the period day 4-26, 2017 are analysed and the Table 3 shows the mean



value of GNSS rays used and coverage rate of voxels penetrated by signals for the test period. It can be concluded from the statistical results (Table 3) that the number of signals used in Scheme 2 is apparently large (doubled to tripled) compared to that of Scheme 1, however, the percentage difference of voxels crossed by rays between Schemes 2 and 1 is not evident except for the case of E-14. The number of Galileo satellite observations is small during the test period, therefore, a low number of signals used and a low coverage rate of voxels penetrated by GNSS signals existed for the case of E-14 in Scheme 1.

Table 3. Number of GNSS rays used and the coverage rate of crossed voxels in different schemes during the experimental period

	Scheme 1				Scheme 2				
	G-14	C-14	R-14	E-14	GC-10	GR-10	CR-10	GCR-10	GRE-10
Number of signals used	974	1123	693	349	1433	1144	1232	1905	2137
Coverage rate of voxels (%)	75.3	71.8	68.0	50.0	73.8	73.6	71.2	76.9	77.4

\*-14 refers to the statistical result with single-GNSS observations derived from fourteen stations

\*-10 refers to the statistical result with multi-constellation GNSS observations derived from ten stations

To analyse the number of SWDs used and the coverage rate of voxels, the average values of two schemes for each day is calculated in Figures 2 and 3, respectively. Figure 2 reveals that the signals used for each day in Scheme 2 is more than double that in Scheme 1: however, Figure 3 reveals that the proportion of voxels penetrated by GNSS signals in Scheme 2 is only about 8% more than that in Scheme 1.

One point should be noted is that the number of Galileo satellite is lower, therefore, we re-analysed the SWD numbers and the coverage rate of voxels after removing the case of E-14 in Scheme 1 (redesignated as Scheme 3). Figures 4 and 5 show the number of SWDS as well as the proportion of voxels penetrated by GNSS signals without considering the Galileo satellites. From Figures 4 and 5 we can conclude that the number of signals used in Scheme 2 remains the greatest at about double that of Scheme 3, but the percentage difference in number of voxels decreased and only about 3% more than that in Scheme 3. Table 4 lists statistical results relating to SWD numbers and the coverage rate of voxels for three Schemes mentioned above. From Table 4 we concluded that, compared to the single-GNSS observations derived from fourteen stations, the percentage of voxels crossed by rays from the multi-constellation GNSS observations of ten stations is only increased by 2.9%. Although multiple GNSS observations have been used in Scheme 2, the coverage rate of voxels did not improve when four stations were removed compared to that of Scheme 1. This reveals that the station density has a more important influence on the coverage rate of voxels crossed by rays than multi-constellation GNSS observations.

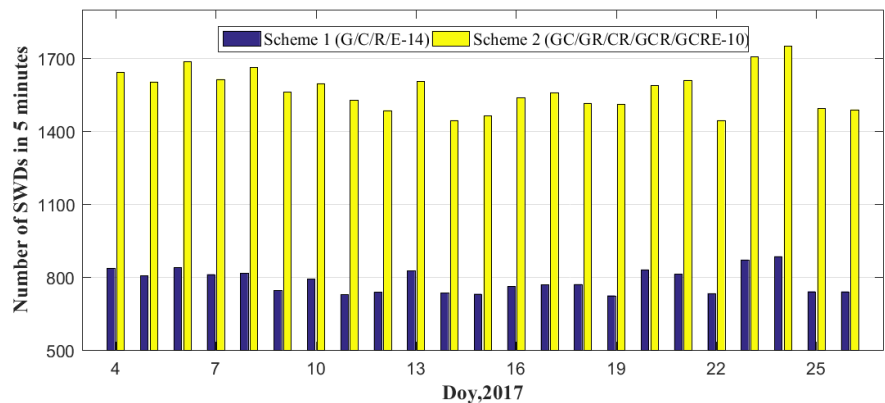


Figure 2. Average number of SWDs used in 5 minutes for two Schemes during the experimental period

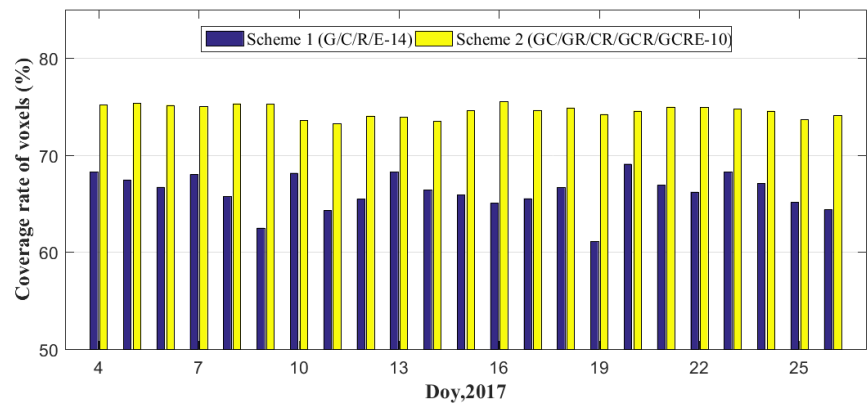


Figure 3. Average coverage rate of voxels penetrated by GNSS signals for two Schemes during the experimental period

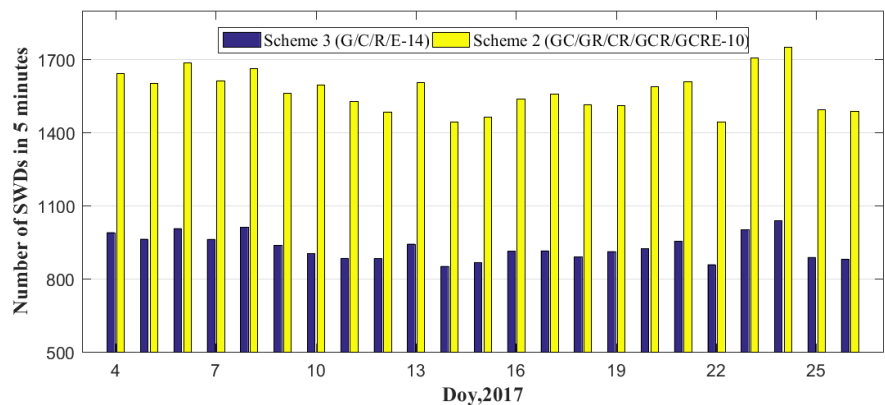


Figure 4. Average number of SWDs used in 5 minutes for Schemes 2 and 3 during the experimental period



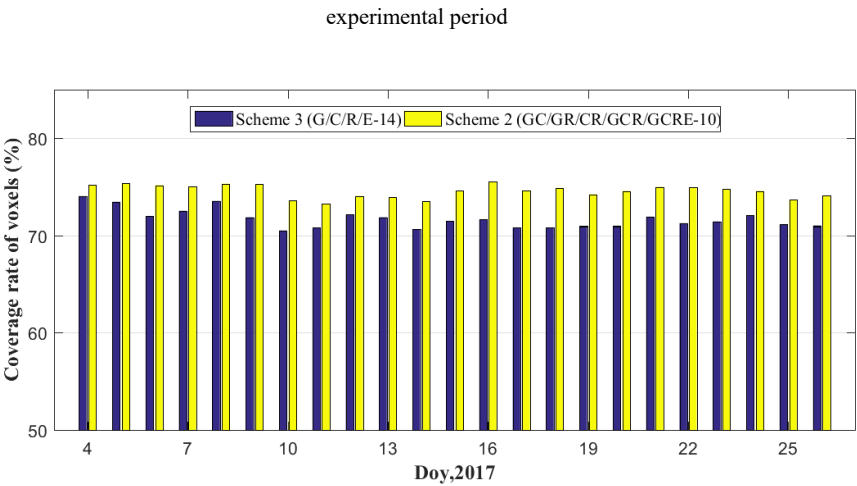


Figure 5. Average coverage rate of voxels penetrated by GNSS signals for Schemes 2 and 3 during the experimental period

Table 4. Statistical information of GNSS signals used and the percentage of voxels penetrated during the tested period

Scheme	Number of signals used	Percentage of crossed voxels (%)
1	785	66.2
2	1570	74.6
3	930	71.7

#### 4.2 Comparison with radiosonde data

In this section, we further compared the influence of station density on the tomographic result. In the experimental area, there is a radiosonde station, as shown by the green circle in Figure 1. Several studies have proved that radiosonde data has a high accuracy in providing the water vapour profiles (Niell et al., 2001; Liu et al., 2013), and the result calculated from radiosonde is used as a reference in this paper to evaluate the tomographic result. The comparison experiment of reconstructed wet refractivity profile information of different Schemes at the radiosonde station with the radiosonde data is carried out at two specific epochs (UTC 00:00 and 12:00, respectively). Figure 6 shows the root mean square (RMS) error of wet refractivity difference between different tomography conditions and radiosonde data. Table 5 gives the specific statistical information pertaining to RMS, bias, and mean absolute error (MAE) for different Schemes. From Figure 6 and Table 5, we can conclude that the tomographic results using different single/multi-constellation GNSS observations are similar at the radiosonde location. As presented in Figure 1, station HKSC is near the radiosonde station, therefore, the reconstructed atmospheric wet refractivity from different cases nearby the location of radiosonde station are relatively accurate and undifferentiated; however, such a result cannot represent the quality of reconstructed results of wet refractivity fields for the entire region. Therefore, the performance of the tomographic result for the entire research region is further evaluated using the PPP-estimated SWDs below.

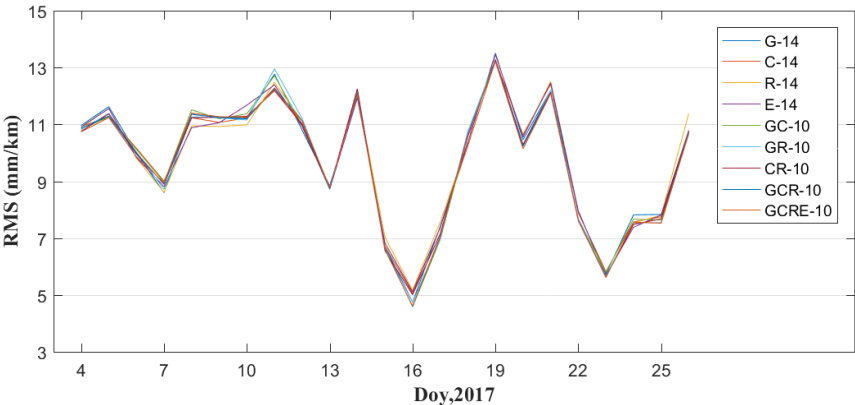


Figure 6. RMS error of wet refractivity difference derived from various conditions during the experiment period

Table 5. Statistical result of RMS, Bias and MAE of wet refractivity difference for different Schemes during the experimental period

Scheme		RMS (mm/km)	Bias (mm/km)	MAE (mm/km)
1	G-14	9.78	1.54	7.12
	C-14	9.78	1.55	7.14
	R-14	9.75	1.64	7.15
	E-14	9.76	1.66	7.14
2	GC-10	9.72	1.40	7.10
	GR-10	9.71	1.40	7.10
	CR-10	9.72	1.46	7.10
	GCR-10	9.68	1.41	7.07
	GCRE-10	9.66	1.42	7.07

### 4.3 Comparison with PPP-estimated SWDs

To assess the reconstructed result of the entire region, two new schemes are designed: Scheme 1, using only the single-GNSS observations from thirteen GNSS stations (except for HKSC) is used for reconstructing the atmospheric wet refractivity; Scheme 2, nine GNSS stations, as shown by the black triangles in Figure 1, are selected using combined multi-constellation GNSS observations. The slant wet delays of station HKSC are computed based on the different tomographic results and their differences against the multi-constellation GNSS PPP-estimated slant wet delays are also obtained. The RMS and MAE of SWD residuals for each day in two schemes are presented in Figures 7 and 8, where the red dashed line represents the average RMS and MAE obtained under conditions G-13, C-13, R-13, and E-13 while the blue dashed line represents the average RMS and MAE obtained from cases GC-9, GR-9, CR-9, GCR-9, and GCRE-9, respectively. Figures 7 and 8 reveal that the average RMS and MAE of Scheme 1 is mostly smaller than that of Scheme 2 over the experimental period, which shows that the reconstructed atmospheric wet refractivity field of Scheme 1 over the entire research area is



superior to the tomographic result of Scheme 2. Statistical results pertaining to different schemes are listed in Table 6, from which it is seen that, compared to Scheme 2, the average RMS and MAE accuracy of Scheme 1 is increased by 16% and 33.4%, respectively. Thence it was concluded that, compared to the tomographic result of multi-constellation GNSS observations, increasing the station density has greater significance to the reconstruction of the atmospheric water vapour field.

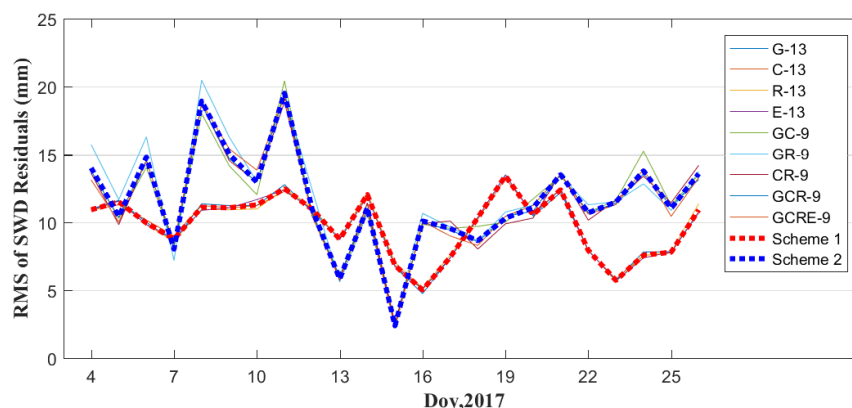


Figure 7. Average RMS of SWD residuals for different schemes over the experimental period

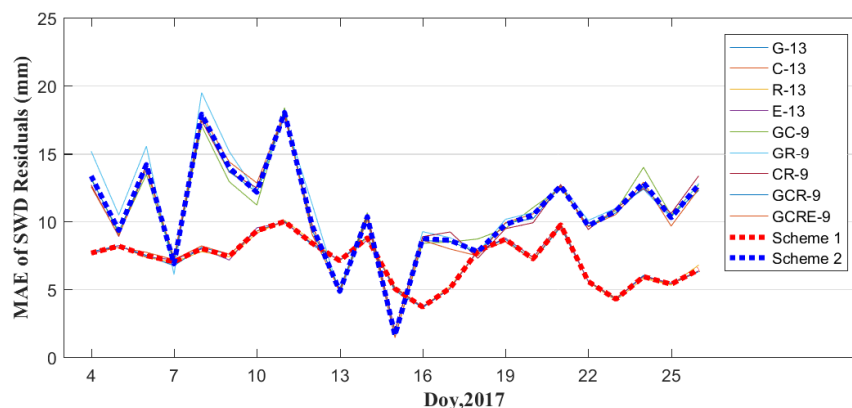


Figure 8. Average MAE of SWD residuals for different schemes over the experimental period

Table 6. Statistical result of RMS and MAE for two schemes over the experimental period

Scheme		RMS	MAE
1	G-14	9.78	7.12
	C-14	9.77	7.14
	R-14	9.79	7.15
	E-14	9.76	7.14
2	GC-10	11.64	10.62
	GR-10	11.99	11.09
	CR-10	11.50	10.66



GCR-10	11.55	10.61
GCRE-10	11.52	10.58

302

## 303 5 Analysis of multi-constellation GNSS troposphere tomography

### 304 5.1 Comparison of signals used and coverage rate of voxels penetrated

305 Here, all fourteen GNSS stations are selected to reconstruct the atmospheric wet refractivity, and  
 306 the tomographic results derived from different multi-constellation GNSS observations are  
 307 compared and analysed. Nine types of single/multi-constellation GNSS observations are designed  
 308 in schemes designated: G-14, C-14, R-14, E-14, GC-14, GR-14, CR-14, GCR-14, and GCR-14,  
 309 respectively. Before evaluating the performance of the tomographic result, the average number of  
 310 GNSS signals used and the percentage of voxels penetrated over the experimental period for each  
 311 tomography step are first analysed (Table 7). Table 7 reveals that compared to schemes G-14 C-14,  
 312 R-14, and E-14, multi-constellation GNSS schemes have more voxels crossed by rays, but the  
 313 change is small with respect to changing SWD numbers.

314

315 Table 7. Statistical information of number of GNSS rays used and the coverage rate of voxels  
 316 penetrated

	G-14	C-14	R-14	E-14	GC-14	GR-14	CR-14	GCR-14	GCRE-14
Number of signals used	974	1123	693	349	2097	1168	1816	2791	3139
Coverage rate of voxels (%)	75.3	71.8	68.0	50.0	80.0	79.8	78.8	82.0	82.4

317

### 318 5.2 Evaluation of multi-constellation GNSS troposphere tomography

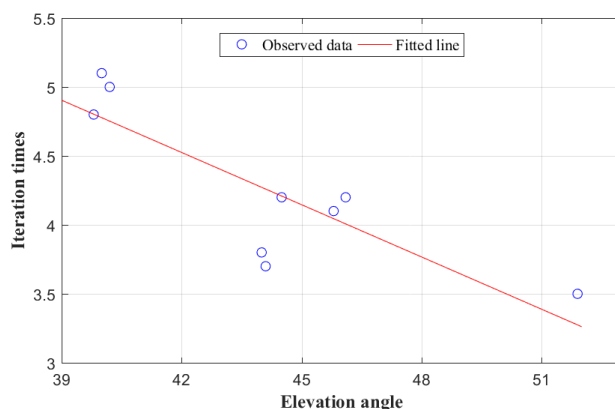
319 To analyse the performance of the multi-constellation GNSS troposphere tomography, the wet  
 320 refractivity profile derived from nine schemes is first compared with the result from the  
 321 radiosonde data thereat. The average RMS, Bias and MAE of wet refractivity difference between  
 322 different schemes and radiosonde data over the experimental period are calculated (Table 8). As  
 323 mentioned in Section 2, an iterative produce is required to determine the weighting matrices of  
 324 different equations in tomographic modelling. Therefore, the number of iterations and the average  
 325 elevation angle of satellite signals for different schemes are also considered (Table 8). It can be  
 326 observed from Table 8 that the average RMS, bias, and MAE of different schemes are similar,  
 327 which reflects the fact that the reconstructed wet refractivity profile obtained from different  
 328 schemes applied at the radiosonde station have equivalent accuracy.  
 329 However, the number of iterations of various schemes are different when determining the  
 330 weighting matrices of the different types of equations used in tomographic modelling. By  
 331 analysing the relationship between the number of iterations and elevation angles over the tested  
 332 period, a negative linear relationship is found between two factors and the fitted data are presented  
 333 in Figure 9. Such a negative correlation reveals that the resolving time of tomographic modelling  
 334 can be decreased with multi-constellation GNSS observations, which is important in the real-time  
 335 reconstruction of atmosphere water vapour data.

336 Table 8. Statistical result of average RMS, Bias, MAE, elevation angle and iteration times for



337

Scheme	RMS	Bias	MAE	Iteration times	Elevation angle (°)
G-14	9.78	1.54	7.12	4.8	39.8
C-14	9.77	1.55	7.14	3.5	51.9
R-14	9.79	1.64	7.15	5.0	40.2
E-14	9.76	1.66	7.14	4.2	44.5
GC-14	9.76	1.54	7.11	4.1	45.8
GR-14	9.75	1.52	7.10	5.1	40.0
CR-14	9.78	1.56	7.14	4.2	46.1
GCR-14	9.76	1.55	7.09	3.8	44.0
GCRE-14	9.75	1.55	7.10	3.7	44.1



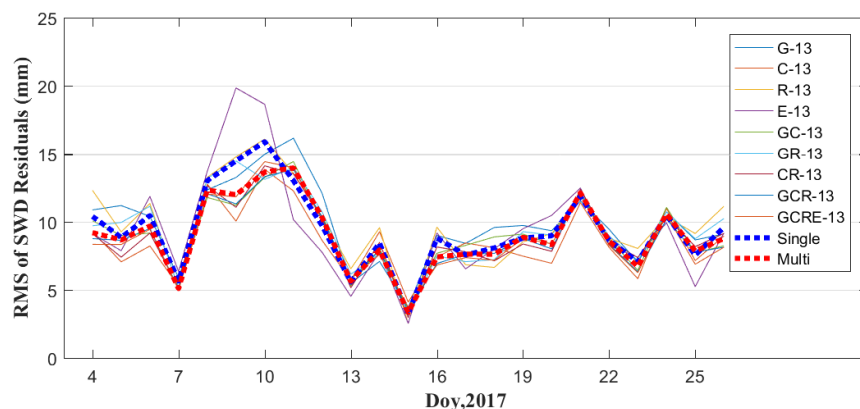
338

339 Figure 9. Relationship between iteration times and elevation angle during the experimental period

340

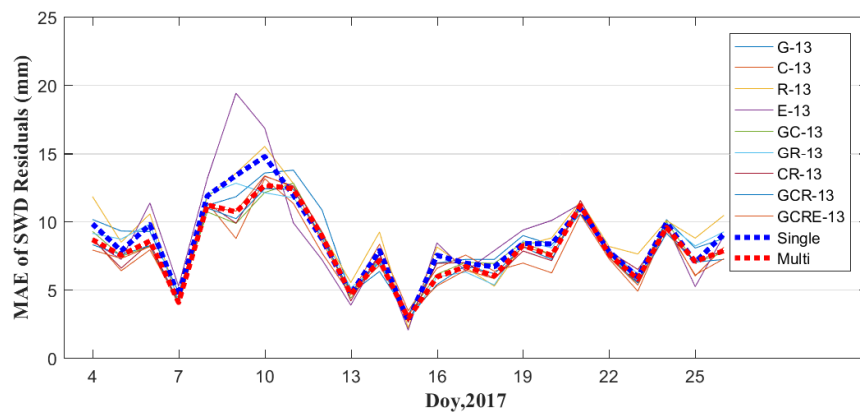
341 As mentioned above, the accuracy of different schemes evaluated for the location of radiosonde  
 342 cannot represent the tomographic quality across the entire region, therefore, a further comparison  
 343 is carried out using only thirteen GNSS stations in the network except for station HKSC. The slant  
 344 wet delays of station HKSC, estimated using multi-GNSS PPP software, are compared with the  
 345 calculated SWDs derived from different schemes. Figures 10 and 11 show the average RMS and  
 346 MAE of SWD residuals on each day during the experiment, where the blue dashed line represents  
 347 the average of RMS and MAE obtained from schemes G-13, C-13, R-13, and E-13, while the red  
 348 dashed line represents the average of RMS and MAE obtained from schemes GC-13, GR-13,  
 349 CR-13, GCR-13, and GCRE-13. From those two Figures it was found that the reconstructed  
 350 quality of atmospheric wet refractivity field data for the entire region using multi-constellation  
 351 GNSS observations has been improved slightly, when compared to that using single-constellation  
 352 GNSS data. By analysing the statistical results pertaining to different schemes (Table 9) it was  
 353 found that, compared to the single-constellation GNSS troposphere tomography, RMS accuracy of  
 354 the multi-constellation GNSS troposphere tomography improved by about 10%.

355



356

357 Figure 10. Average RMS of SWD residuals for different schemes over the experimental period



358

359 Figure 11. Average MAE of SWD residuals for different schemes over the experimental period

360 Table 9. Statistical result of RMS, Bias and MAE of SWD residuals from different schemes over  
 361 the experimental period

Scheme	RMS	Bias	MAE
G-13	9.83	6.71	8.62
C-13	8.58	6.34	8.58
R-13	9.05	7.65	9.05
E-13	9.41	7.62	8.83
GC-13	9.03	6.44	7.96
GR-13	9.40	6.66	8.28
CR-13	8.89	6.78	7.96
GCR-13	8.78	6.38	7.77
GCRE-13	8.75	6.36	7.73

362

## 363 6 Conclusion

364 The observed multi-constellation GNSS (GPS, BeiDou, GLONASS, and Galileo) observations



have been used to investigate the importance and influence of station density and multi-GNSS constellation data on troposphere tomography. The SWDs of fourteen GNSS stations in a network in Hong Kong are estimated using the multi-constellation GNSS PPP software. For GNSS troposphere tomography, the horizontal resolution of voxels is first determined according to the number of voxels and the coverage rate of GNSS stations located in the bottom layers. A comparative experiment using single/multi-constellation GNSS data derived from different numbers of stations revealed that increasing the station density improved the quality of tomographic results with the RMS accuracy of SWDs residuals increasing by about 16%, when compared to the result obtained when using multi-constellation GNSS troposphere tomography. In addition, compared to the single-constellation GNSS observations, troposphere tomography using multi-constellation GNSS data can: (1) reduce the resolving time when determining the weighting matrices of different equations used in tomographic modelling, which has practical significance for the real-time reconstruction of atmospheric water vapour profiles; and (2) improve the quality of tomographic results to a certain extent. With the upcoming full operability of the multi-constellation GNSS, it is expected to increase the number of SWDs used for troposphere tomography. Although the improvement of reconstructed results is not as was expected, it was mainly determined by the spatial distribution of GNSS stations, multi-constellation GNSS troposphere tomography is also worth studying, especially for potential application of this technique in real-time atmospheric water vapour reconstruction.

**Acknowledgments:** The authors thank IGAR (Integrated Global Radiosonde Archive) for providing the radiosonde data. The Lands Department of HKSAR and Hong Kong Observatory are also acknowledged for providing GNSS and the corresponding meteorological data. This research was funded by the State Key Program of National Natural Science Foundation of China (41730109).

**Conflicts of Interest:** The authors declare no conflict of interest.

## References

- [1] Bartlett, M. S.: Properties of Sufficiency and Statistical Tests. In Proc. R. Soc. London A 160, 268-282, 1937.
- [2] Bender M., and Raabe A.: Preconditions to ground based GPS water vapour tomography Annales geophysicae, 25(8): 1727-1734, 2007.
- [3] Bender, M., Dick, G., Ge, M., Deng, Z., Wickert, J., Kahle, H. G., Raabe, A., and Tetzlaff.: Development of a gnss water vapour tomography system using algebraic reconstruction techniques. Advances in Space Research, 47(10), 1704-1720, 2011.
- [4] Bender, M., Stosius, R., Zus, F., Dick, G., Wickert, J., and Raabe, A.: GNSS water vapour tomography–Expected improvements by combining GPS, GLONASS and Galileo observations. Advances in Space Research, 47(5), 886-897, 2011.
- [5] Benevides, P., Catalao, J., and Miranda, P. M. A.: On the inclusion of gps precipitable water vapour in the nowcasting of rainfall. Natural Hazards & Earth System Sciences, 3(6), 3861-3895, 2015a.
- [6] Benevides, P., Nico, G., Catalao, J., and Miranda, P.: Can Galileo increase the accuracy and



- 408 spatial resolution of the 3D tropospheric water vapour reconstruction by GPS tomography? In  
409 Geoscience and Remote Sensing Symposium (IGARSS), 2015 IEEE International, 3603-3606,  
410 2015b.
- 411 [7] Benevides, P., Nico, G., Catalão, J., and Miranda, P. M. A.: Analysis of galileo and gps  
412 integration for gnss tomography. *IEEE Transactions on Geoscience & Remote Sensing*, 55(4),  
413 1936-1943, 2017.
- 414 [8] Benevides, P., Catalao, J., and Nico, G.: Inclusion of high resolution MODIS maps on a 3D  
415 tropospheric water vapor GPS tomography model. *Remote Sensing of Clouds and the Atmosphere*.  
416 International Society for Optics and Photonics, 9640, 96400R-1-96400R-13, 2015.
- 417 [9] Bi, Y., Mao, J., and Li, C.: Preliminary results of 4-D water vapor tomography in the  
418 troposphere using GPS. *Advances in atmospheric sciences*, 23(4), 551-560, 2006.
- 419 [10] Champollion, C., Masson, F., Bouin, M. N., Walpersdorf, A., Doerflinger, E., Bock, O., and  
420 Van Baelen, J.: GPS water vapour tomography: preliminary results from the ESCOMPTE field  
421 experiment. *Atmospheric research*, 74(1), 253-274, 2005.
- 422 [11] Chen, B. Y., and Liu, Z. Z.: Voxel-optimized regional water vapor tomography and  
423 comparison with radiosonde and numerical weather model. *Journal of Geodesy*, 88(7), 691-703,  
424 2014.
- 425 [12] Crespi, M. G., Luzietti, L., and Marzario, M.: Investigation in gnss ground-based  
426 tropospheric tomography: benefits and perspectives of combined galileo, glonass and gps  
427 constellations. *Geophysical Research Abstracts*, 10, EGU2008-A-03643, 2008.
- 428 [13] Flores, A., Ruffini, G., and Rius, A.: 4D tropospheric tomography using GPS slant wet delays.  
429 *Annales Geophysicae*, 18(2), 223-234, 2000.
- 430 [14] Guo, J., Yang, F., Shi, J., and Xu, C.: An Optimal Weighting Method of Global Positioning  
431 System (GPS) Troposphere Tomography. *IEEE Journal of Selected Topics in Applied Earth*  
432 *Observations and Remote Sensing*, 9(12), 5880-5887, 2016.
- 433 [15] Liu, Z., Wong, M. S., Nichol, J., and Chan, P. W.: A multi-sensor study of water vapour from  
434 radiosonde, MODIS and AERONET: a case study of Hong Kong. *International Journal of*  
435 *Climatology*, 33(1), 109-120, 2013.
- 436 [16] Niell, A. E., Coster, A. J., Solheim, F. S., Mendes, V. B., Toor, P. C., Langley, R. B., and  
437 Upham, C.: A. Comparison of measurements of atmospheric wet delay by radiosonde, water vapor  
438 radiometer, GPS, and VLBI. *Journal of Atmospheric and Oceanic Technology*, 18(6), 830-850,  
439 2001.
- 440 [17] Nilsson, T., and Gradinarsky, L.: Water vapor tomography using gps phase observations:  
441 simulation results. *IEEE Transactions on Geoscience & Remote Sensing*, 44(10), 2927-2941,  
442 2006.
- 443 [18] Notarpietro, R., Cucca, M., Gabella, M., Venuti, G., and Perona, G.: Tomographic  
444 reconstruction of wet and total refractivity fields from gnss receiver networks. *Advances in Space*  
445 *Research*, 47(5), 898-912, 2011.
- 446 [19] Radon, J.: Über die bestimmung von funktionen durch ihre in-te-gral-werte längs gewisser  
447 mannigfaltigkeiten. *Computed Tomography*, 69, 262-277, 1917.
- 448 [20] Rohm, W., and Bosy, J.: Local tomography troposphere model over mountains area.  
449 *Atmospheric Research*, 93(4), 777-783, 2009.
- 450 [21] Skone, S., and Hoyle, V.: Troposphere modeling in a regional gps network. *Positioning*,  
451 4(1&2), 230-239, 2005.





- 452 [22] Troller, M., Bürki, B., Cocard, M., Geiger, A., and Kahle, H. G.: 3-d refractivity field from  
453 gps double difference tomography. *Geophysical Research Letters*, 29, 2149–2152, 2002.
- 454 [23] Troller, M., Geiger, A., Brockmann, E., Bettems, J. M., Bürki, B., and Kahle, H. G.:  
455 Tomographic determination of the spatial distribution of water vapor using GPS observations.  
456 *Advances in Space Research*, 37(12), 2211–2217, 2006.
- 457 [24] Wang, X., Dai, Z., Wang, L., Cao, Y., and Song, L.: Preliminary Results of Tropospheric Wet  
458 Refractivity Tomography Based on GPS/GLONASS/BDS Satellite Navigation System. In *China*  
459 *Satellite Navigation Conference (CSNC) Proceedings: Volume I*, 1–7, 2014.
- 460 [25] Yao, Y. B., and Zhao, Q. Z.: A novel, optimized approach of voxel division for water vapor  
461 tomography. *Meteorology and Atmospheric Physics*, 129(1), 57–70, 2016a.
- 462 [26] Yao, Y. B., and Zhao, Q. Z.: Maximally Using GPS Observation for Water Vapor Tomography.  
463 *IEEE Transactions on Geoscience and Remote Sensing* 54(12), 7185–7196, 2016b.
- 464 [27] Yao, Y. B., Zhao, Q. Z., and Zhang, B.: A method to improve the utilization of GNSS  
465 observation for water vapor tomography. *Annales Geophysicae*, 34(1), 143–152, 2016.
- 466 [28] Zhao, Q. Z., Yao, Y. B., Cao, X. Y., Zhou, F., and Xia, P.: An optimal tropospheric  
467 tomography method based on the multi-gnss observations. *Remote Sensing*, 10(2), 1–15, 2018.
- 468 [29] Zhao Q. Z., and Yao Y. B.: An improved troposphere tomographic approach considering the  
469 signals coming from the side face of the tomographic area. In *Annales Geophysicae*, 35(1), 87–95,  
470 2017.